Article

Extended switching endurance of phase change memory through nano-confined cell structure

Check for updates

Jia Zheng[1,2], Ruobing Wang[1], Wencheng Fang[1], Chengxing Li [1], Jiarui Zhang[1], Ziqi Wan[1], Yuqing Chen[1], Jin Liu[1], Xixi Zou[1], Li Xie[1], Qian Wang[1], Xi Li[1], Sannian Song[1], Xilin Zhou [1] ✉ & Zhitang Song [1] ✉

Phase change memory has been regarded as a promising candidate for storage class memory application. However, the high switching current and limited switching endurance remain a critical challenge. In this work a switching endurance beyond 1.1×10^{11} cycles is demonstrated in the mushroom-type memory device with nano-cofined structure and carbon-doped GeSbTe material. The over-programming of the memory cell induced by excessive RESET current gives rise to the recrystallization of the active phase change volume which accelerates the inward migration of carbon atoms to the bottom heater. The cyclic switching exacerbates the over-programming effect with denser carbon cluster accumulated at the boundary of the active region which causes the stuck-RESET failure. The nano-confined cell structure enables efficient heating by relocating the melt-quench region away from the interface to the dielectric layer which substantially reduces the RESET energy and, consequently, mitigates the over-programming effect and significantly extends the switching cycles.

The data storage technology has received great progress in the past decades due to the growing favor of edge-end smart devices, automotive electronics, and large-scale machine learning models[1–5]. Phase change memory (PCM) is considered one of the most promising candidates for data storage and memory applications due to its rapid and reversible memory switching characteristics[6], large resistance ratio[7,8], and high integration density[9]. However, the limitation on cyclic switching endurance puts an obstacle to the wide adoption of PCM as storage-class memory (SCM). The reported data shows that many PCM devices exhibit endurance limits in the range of 1×10^6 to 1×10^9 cycles for the mushroom-type structure[10–12], the confined PCM structures by atomic layer deposition (ALD) process have been reported exceeding 1×10^{12} cycles[13–15]. The PCM cells in a mushroom-type structure are known for their high thermal stability, good process compatibility, fast switching capability, and cost-effectiveness[7,16].

In the embedded PCM applications, such as those observed in automotive systems, phase change materials are typically employed with elemental dopants to improve the thermal stability at high temperature[17,18]. The introduction of dopants into phase change materials effectively reduces volume change during phase transitions, thereby mitigating the thermal stress experienced by the phase change layer (PCL) during cyclic switching[18,19]. Dopants increase the crystallization temperature of the phase change material, which helps prevent void formation-a key factor contributing to stuck-RESET failure in PCM devices[20]. The carbon doping in GeSbTe suppresses grain nucleation and crystal growth, minimizing structural degradation while simultaneously increasing resistivity to lower the RESET current. Moreover, it enhances the thermal stability of the amorphous phase, effectively inhibiting crystallization kinetics and significantly improving high-temperature data retention[18,19]. The continuous atomic motion due to wind forces and incongruent melting processes in the

[1]State Key Laboratory of Materials for Integrated Circuits, Shanghai Institute of Microsystem and Information Technology, Chinese Academy of Sciences, Shanghai, China. [2]University of Chinese Academy of Sciences, Beijing, China. ✉e-mail: xilinzhou@mail.sim.ac.cn; ztsong@mail.sim.ac.cn

memory switching presents a critical challenge on the endurance performance which ultimately leads to stuck-RESET bits[10,21–25]. The challenge is particularly complex for the doped phase change material if the doped atoms are not in favor of bonding with the constituent elements of the phase change materials, such as germanium, antimony, and tellurium of GeSbTe material.

The nanoscale confined cell structures have been used in PCM devices due to the good compositional uniformity and high heating efficiency[9,26]. The endurance of the confined PCM cells exceeds 1×10^{12} cycles by adopting a symmetric nano-pillar cell and self-void healing mechanism through a metallic linear that enables an alternative conductive path[13–15]. The deposition of uniform phase-change materials by ALD is crucial for the fabrication of nanopillar confined structures[27–30], in which the deposition of phase change material is completed by saturature surface reactions of the precursor with reactive surface bonds[14,31]. The endeavor to ensure compositional uniformity of multicomponent phase change alloys is challenging due to the limitations in precursor preparation and controlling of precursor reaction process[32,33]. Furthermore, the ALD deposition is accompanied by the presence of by-products and residuals, which potentially introduce contamination in the PCM cells[34,35]. On the other hand, the typical patterning process for confined cells by subtractive etching gives rise to the issues of overlay inaccuracy and etching damage of chalcogenides, which results in cell-to-cell variation in the reset switching current[36–39]. The over-programming effect is therefore presented in parts of PCM cells, given the utilization of a consistent programming current across the memory array[40–43]. The bottom heater of the PCM cell normally shows high thermal conductivity which serves as an effective heat sink for the thermal dissipation and provides enhanced tolerance to over-programming[44,45]. However, in the conventional mushroom-type PCM cell where PCL is in contact with the bottom heater that is surrounded by the dielectric material the void formation is observed at the PCL/dielectrics interface after the plasma etching and wet cleaning process which is due to the poor adhesive strength of phase change material[23,46]. The interface is degraded under cyclic switching with regular thermal and electrical stress[47,48].

Previous works on PCM cells with confined structures have encountered several challenges, such as the difficulty in maintaining compositional uniformity during ALD, the introduction of by-products and contamination, and overlap issues related to patterning. In this study, the proposed nano-confined structure overcomes these limitations by providing a scalable and material-flexible solution with enhanced thermal stability and optimized switching characteristics. The PCM devices with nano-confined cell structure in a wafer-level memory array are demonstrated with advantages of low switching current, fast programming speed, and long cyclic switching endurance. The nano-confined PCM cell is fabricated based on the mushroom-type structure, which incorporates the physical vapor deposition and subtractive plasma etching of phase change material, by which the switching cycles are substantially extended by more than three orders of magnitude without adding complexity to the manufacturing process. Moreover, it allows for the deposition of phase change materials with higher compositional flexibility via physical vapor deposition (PVD), enabling improved thermal stability, reduced resistance drift, and tunable phase change kinetics. The robust switching endurance, together with the high thermal stability using carbon-doped GeSbTe (CGST) phase change material, is benefited from the nano-confined structure, which enables the high efficient Joule heating and effectively addresses the issue of over-programming effect induced by the excessive RESET energy in the cyclic switching. The over-programming in the PCM cell intensifies the composition segregation of the active phase change volume and consequently accelerates the degradation of reversible switching performance, in which the massive carbon segregation is identified as the dominant factor for the failure of cyclic switching. The improved heating

efficiency plays an essential role in reducing the programming energy, which mitigates the occurrence of the over-programming effect by utilizing a designed RESET programming scheme with reduced energy. The switching endurance is significantly extended from 3×10^8 cycles to more than 1.1×10^{11} cycles for the mushroom-type PCM cell, which is close to the state-of-the-art endurance performance of confined PCM devices.

The ex situ micro-structural analysis of the PCM cells reveals that the carbon segregation is accumulated at the boundary of a dome-like active region in the CGST material which effectively confines and stabilizes the active phase change volume of PCL in a three-dimensional geometry, thus contributing to a reliable memory switching with high energy efficiency and long switching cycles.

Results

Switching performance of wafer-level nano-confined PCM cells

Figure 1a–d presents the schematic illustration of the mushroom-type PCM cells with a sandwiched structure of the bottom heater, PCL, and TiN top electrode contact. The programming pulse from the heater facilitates the reversible structural transformation between the amorphous and crystalline states. The RESET pulse induces a short and intense heating process, resulting in a rapid cooling of the active region and the subsequent transformation of phase change material into an amorphous state, which is characterized by a high-resistance state (HRS). In contrast, the SET process involves a long stepped pulse, leading to the recrystallization of the phase change material with a low resistance state (LRS). The cartoons of PCM device in Fig. 1a, c present the conventional mushroom-type structures with flat heater in contact to the bottom of PCL where the active phase change region locates at the boundary of the PCL, as highlighted in orange. Fig. 1b, d illustrate the nano-confined structure of PCM cell proposed in this work, in which the top of the heater is embedded in the PCL. The structural transition thus occurs inside the PCL where the active region is located above the PCL boundary as shown in Fig. 1d. The transmission electron microscopy (TEM) image in Fig. 1e and the corresponding bright-field scanning transmission electron microscopy (BF-STEM) image in Fig. 1f present the cross-sectional structures of the nano-confined PCM cell in the wafer-level arrays, in which the presence of a dome-like active region is observed which is away from the interface to the dielectric layer in the device after the wafer-level measurement of hundreds of switching cycles. The nano-confined PCM cell exhibits a distinct characteristic where the active phase change region is surrounded by chalcogenide material of low thermal conductivity in all directions, which consequently enhances the heating efficiency significantly of the devices by preventing the thermal dissipation from the interface to the dielectric layer. The improved thermal heating is therefore reached in the nano-confined PCM cell in RESET programming compared to the conventional structure, as depicted by the finite element analysis results shown in Fig. 1g, in which the position of peak temperature in the nano-confined PCM cell moves further into the PCL. The embedded heater delivers Joule heat to the inner part of the phase change materials instead of the interface, which improves the heating efficiency of the RESET programming and hence increases the temperature inside the PCL of the nano-confined structure considerably, as shown in the simulation results of temperature distribution of the PCM cells in Fig. 1h, i. The introduction of the nano-confined structure thus facilitates the RESET programming to HRS of the PCM cell at a reduced current.

To quantitatively evaluate the advantage of the PCM cell with a nano-confined structure over the conventional structure, we analyze the cell resistance as a function of RESET current under various pulse widths for both structures, as shown in Fig. 2a, b. CGST phase change material is used in the devices. Fig. 2a presents the screening results of the duration-current-resistance mapping in the RESET program of 112 nano-confined PCM cells, in which a RESET current of 500 μA and 7 ns
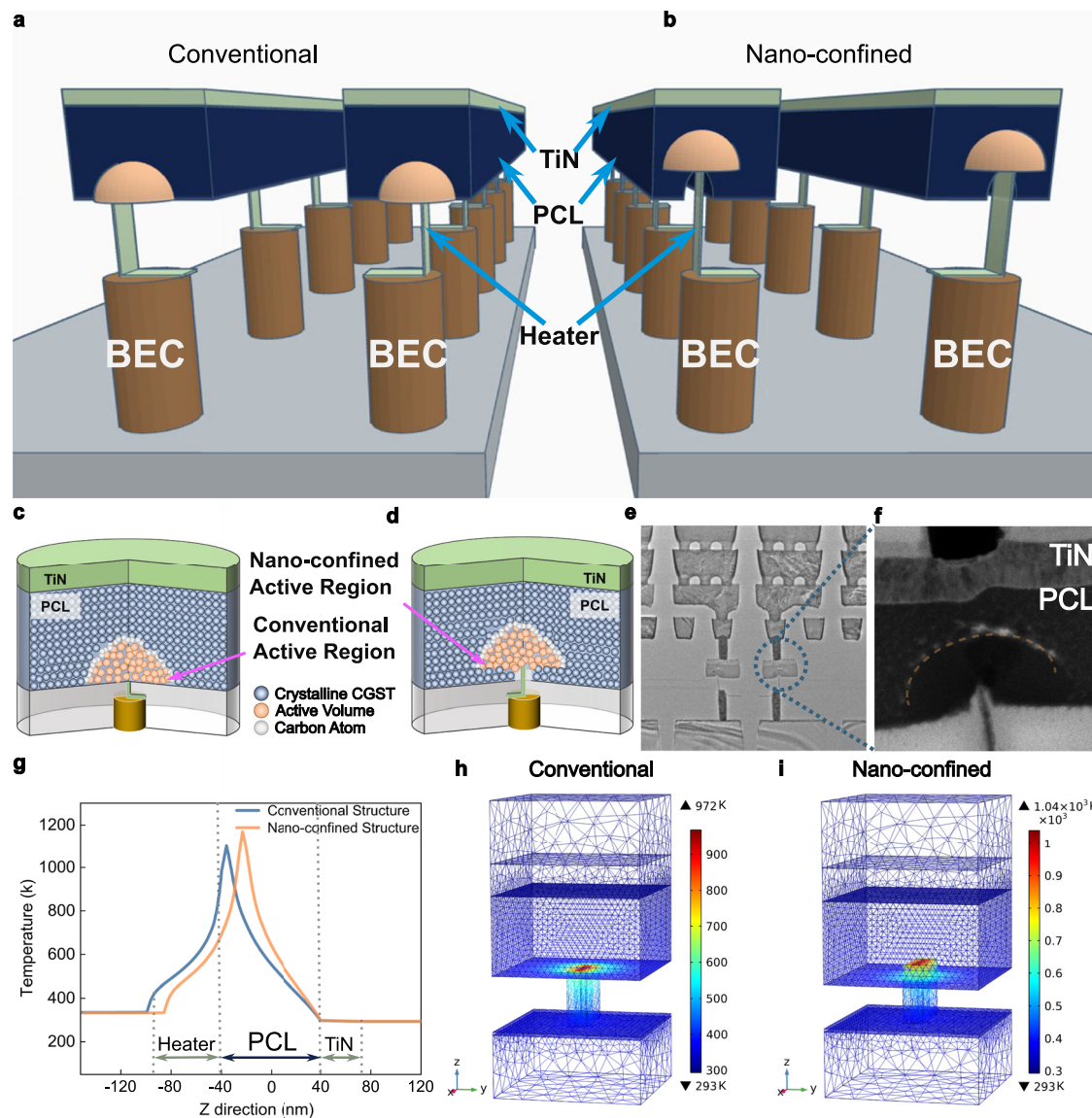
Fig. 1 | Structural comparison and thermal analysis of conventional and nano-confined phase change memory (PCM) cells. a–d Schematic illustration of the PCM cells, where the phase change layer (PCL) is sandwiched between the top TiN electrode and bottom heater, with each PCM cell connected to a controll circuit for individual device access through bottom electrode contact (BEC). **a, c** Conventional PCM cell structure with a flat TiN heater in direct contact with the PCL. **b, d** Nano-confined PCM cell structure, where the top of the TiN heater is embedded in the PCL, shifting the active switching region into the interior of the phase change material. **e** Cross-sectional transmission electron microscopy image of PCM devices subjected to cyclic tests. **f** Magnified cross-sectional bright-field scanning transmission electron microscopy image of a single PCM cell where the active switching region is outlined by dash curve locates above the lower boundary of PCL. **g** Finite element simulation of temperature distribution along the z-direction of PCM cell (from the bottom heater to top TiN electrode) after applying the RESET programming pulse. **h, i** Temperature distribution simulations of conventional and nano-confined PCM cells, respectively, which demonstrate that the nano-confined structure enhances heating efficiency within the PCL by ~50%, leading to reduced RESET current and improved endurance.

is able to program the HRS of PCM cells, while a RESET current of 900 μA is required to reach the HRS in the conventional PCM cells, see Fig. 2b. The standard deviation of the HRS resistance of PCM cells is shown in Fig. S1 in Supplementary Information. As an identical current of larger than 500 μA is applied in the RESET programming, a higher resistance state is achieved in the nano-confined structure due to the improved thermal efficiency. By adopting the embedded heater, the Joule heating in the RESET process becomes increasingly concentrated within the phase change materials. The thermal dissipation through the interface between the phase change and dielectric layer is suppressed, which favors the formation of a mushroom-shaped amorphous volume inside the PCL at a reduced RESET current. The improved energy efficiency of the nano-confined structure is demonstrated in the SET programming as well, in which a higher RESET/SET resistance ratio of up to more than two orders of magnitude is achieved in the nano-confined structure, as shown in Figs. S2 and S3 in Supplementary Information. A smaller SET current is required to reach the minimum resistance of the PCM cells with nano-confined structure, indicating an energy-efficient process for the recrystallization of phase change materials.

The nano-confined structure is considered to be a critical factor in increasing the heating efficiency of RESET programming, as plotted in Fig. 2a, b. To investigate the impact of the increasingly reduced RESET energy on the endurance performance of the PCM cells, a series of switching endurance measurements are performed utilizing tailored RESET programming scheme with variety of RESET pulses from RESET pulse A to pulse H, where the programming RESET energy is decreased continuously, as shown in Fig. 2c–j. The endurance limits of nano-
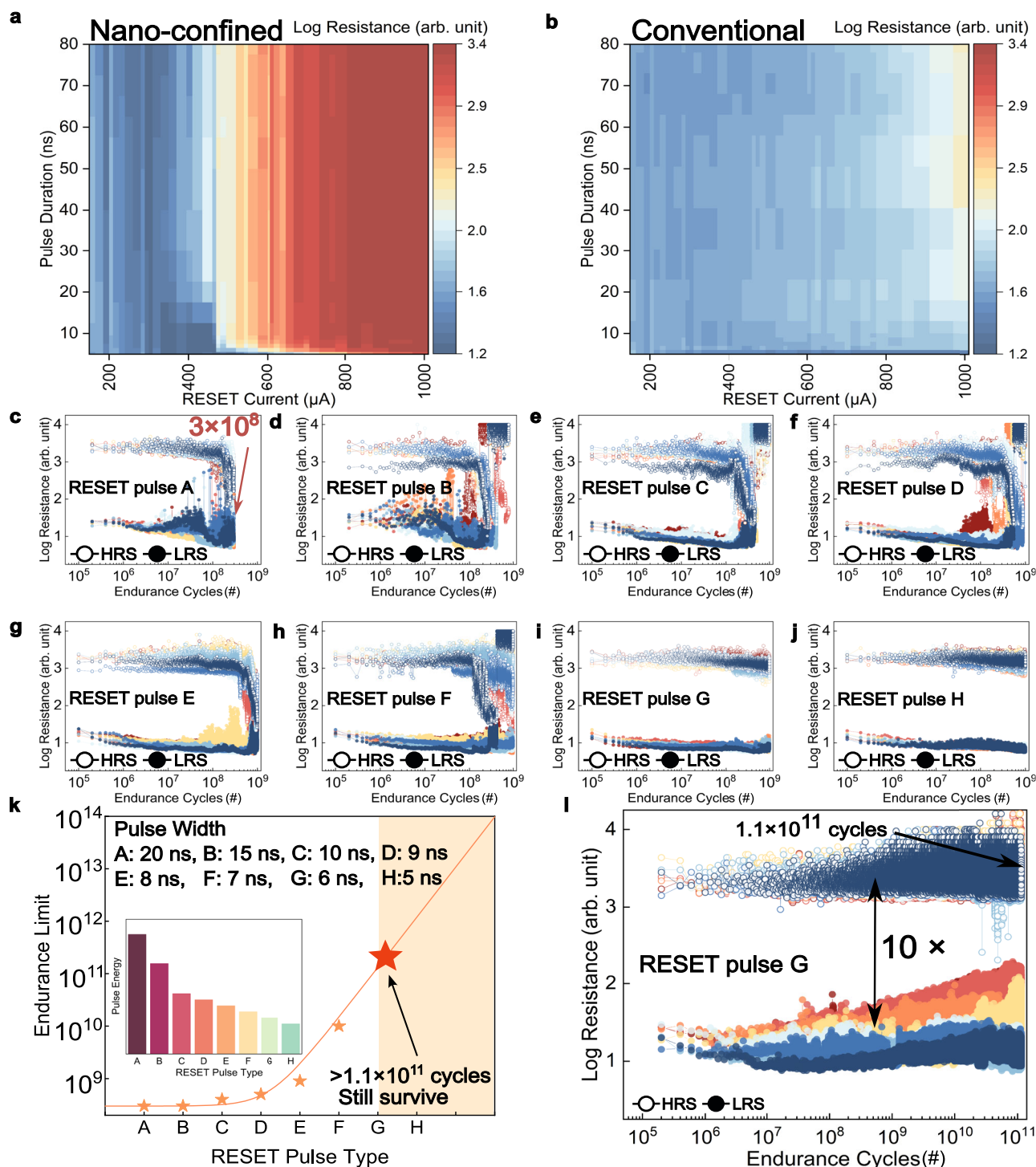
Fig. 2 | RESET programming mapping and endurance performance of nano-confined and conventional phase change memory (PCM) cells. a, b Duration-current-resistance mapping during RESET programming for 112 PCM cells with (**a**) nano-confined and (**b**) conventional cell structures. **c–j** Endurance performance of nano-confined PCM cells using RESET pulses A to H, respectively, which demonstrate endurance up to 1×10^9 cycles with a strong dependence on RESET pulse energy. **k** Endurance limit of PCM cells as a function of RESET pulse, where the inset histogram illustrates the decreasing pulse energy from RESET pulses A–H. **l** Demonstration of switching endurance exceeding 1.1×10^{11} cycles with a resistance ratio greater than 10 under RESET pulse G. The endurance data presented in this figure is measured from eight nano-confined PCM cells, which is representative of more than 8000 tested PCM cells. The current of RESET pulses is fixed at 1000 µA and a constant SET pulse of 440 ns, 400 µA is used in this work. HRS high-resistance state, LRS low-resistance state.

confined structure PCMs under RESET pulses A to G is significantly better than those of conventional structure, which exhibits a switching endurance of ~1×10^6 cycles, as shown in Fig. S4 of Supplementary Information. Moreover, even with extended RESET pulse duration of 80 ns, the memory window of conventional structures remains limited

to approximately one order of magnitude, whereas the nano-confined structure achieves a well separated HRS and LRS in the cyclic switching.

A noticeable decrease in the cell resistance of the PCM cells in HRS is observed as the switching cycle increases under the RESET pulse A to pulse F. The cyclic switching is ended with a stuck-RESET failure before
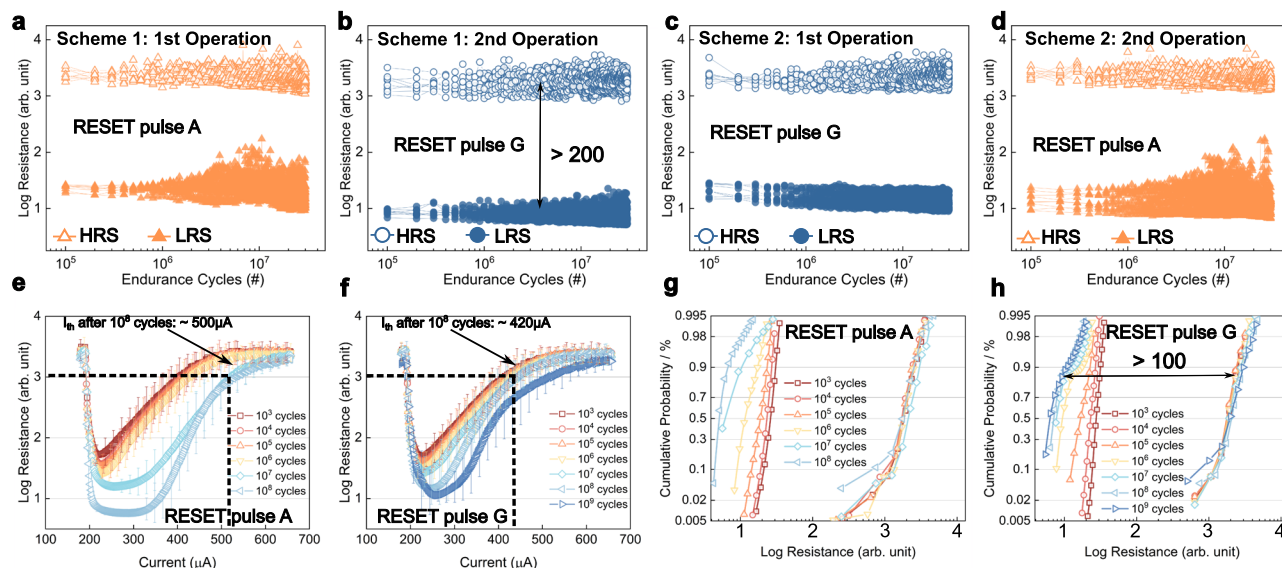
Fig. 3 | Switching performance and resistance distribution of nano-confined phase change memory (PCM) cells under different RESET endurance programming schemes. a, b Endurance cycling of 8 nano-confined PCM cells under scheme 1, showing (**a**) the first 3×10^7 cycles with RESET pulse A, followed by (**b**) an additional 3×10^7 cycles with RESET pulse G, which results in an improved resistance distribution of the LRS. **c, d** Endurance cycling with sequence reversed under scheme 2, with (**c**) the first 3×10^7 cycles using RESET pulse G, followed by **d** the second 3×10^7 cycles under RESET pulse A, which presents significantly increased

LRS fluctuation. The extended cyclic operations are provided in Figs. S5 and S6 in Supplementary Information. **e, f** Resistance-current (R-I) curves of 112 PCM cells after different endurance cycles with (**e**) RESET pulse A and (**f**) RESET pulse G. The threshold current (I_{th}) for the RESET transition is marked by dashed lines. **g, h** Statistical resistance distribution of the high resistance state (HRS) and low resistance state (LRS) for 8192 PCM cells subjected to endurance cycling with (**g**) RESET pulse A and (**h**) RESET pulse G, highlighting the differences in resistance variability over time.

the switching endurance reaches 1×10^9 cycles, which is associated with the pronounced fluctuations in the cell resistance of LRS, as plotted in Fig. 2c–h. As the programming energy decreases further, as shown in Fig. 2i, j, the switching endurance is extended significantly beyond 1×10^9 cycles, in which the cell resistance is well separated, showing around two orders of magnitude difference under RESET pulse G and pulse H. The rapid degradation of cell resistance in both HRS and LRS as the switching endurance beyond 1×10^8 cycles is observed in the PCM cells under RESET pulse A to pulse F. The wild fluctuation in cell resistance is mitigated as the RESET energy is decreased under RESET pulse G and pulse H, which is due to the significant improvement of thermal efficiency of the device and the resultant considerably suppressed over-programming effect in the PCM cell. Fig. 2k illustrates the switching cycle life of the nano-confined PCM cell under different RESET pulses, in which the programming energy of the RESET pulse is shown in the inset. The endurance limit of the PCM cells is extended substantially as the RESET programming energy decreases. The switching endurance beyond 1.1×10^{11} cycles is observed in the nano-confined PCM cells under the RESET pulse G, in which the resistance ratio is more than one order of magnitude, as shown in Fig. 2l. The PCM cells are still in the cyclic programming measurement and the endurance limit has not yet reached due to the time consuming test procedure. A greater extended endurance cycle is therefore expected under the RESET pulse H with further reduced programming energy.

The over-programming effect in RESET switching of the nano-confined PCM cell

To further investigate the impact of the RESET programming energy on the switching performance of PCM cells, the cyclic programming is designed using alternate RESET pulses with high energy RESET pulse A first for 3E7 cycles (scheme 1, see Fig. 3a) followed by low energy RESET pulse G for another 3E7 cycles (see Fig. 3b). Since the pulse parameters for RESET pulse A to pulse G are different, each endurance test requires separate configuration of the circuit, which takes

approximately 3 minutes. The LRS of the PCM cells displays a significant fluctuation as the switching cycle increases in the first programming with RESET pulse A as shown in Fig. 3a, which, whereas, exhibits a stable resistance level in the extra cyclic programming under RESET pulse G with the resistance ratio larger than 200 as plotted in Fig. 3b. On the other hand, when the pulse sequence applied to the PCM cell is reverse, that is, the PCM cells are cyclically programmed using RESET pulse G first, the LRS of the devices present minimum fluctuations up to 3E7 cycles (scheme 2, see Fig. 3c). While the additional 3E7 cycles switching with RESET pulse A is found with noticeably increased fluctuations in LRS, as shown in Fig. 3d. The endurance switching programming with alternate RESET pulses A and pulse G is cyclically performed on the PCM cells until the failure of the devices, as given in Figs. S5 and S6 in Supplementary Information, in which the endurance characteristic under two sets of endurance programming scheme by alternated RESET pulses A and pulse G is presented. The endurance limit of the PCM cells under both of the programming sets is higher than that programmed solely by RESET pulse A. It illustrates that the endurance degradation, including resistance decrease and fluctuation with cycles, under different pulse schemes, is independent of the programming history of the cells. The RESET pulse A accelerates the degradation of the PCM cells due to the over-programming effect, while the RESET pulse G, with reduced energy, is able to cure the degraded cells.

By applying the current pulse with fixed pulse width and increasing amplitude, a reversible phase transition occurs between the HRS and LRS of PCM cells after different switching cycles, as shown in Fig. 3e, f. The threshold current (I_{th}) for the RESET transition with RESET Pulse A and pulse G are both ~400 μA for the PCM cells that experienced up to 1×10^6 switching cycles. However, the I_{th} under RESET pulse A increases significantly as the switching endurance exceeds 1×10^7 cycles, in which a current of 500 μA is required to RESET the PCM cells after 1×10^8 endurance cycles. Whilst for the PCM cells under RESET Pulse G, the I_{th} increases slightly to 420 μA. Furthermore, a substantial decrease in cell resistance of the LRS is observed for the PCM cells under RESET pulse A

as the switching endurance exceeds 1×10^7 cycles. Under RESET pulse G, the I_{th} of the PCM cells remains well below 500 μA even after 1×10^9 endurance cycles, which is presented with a tolerable decrease in cell resistance of the LRS.

The resistance distributions shown in Fig. 3g, h are based on more than 8000 PCM cells after the corresponding switching endurance programming. As the switching endurance exceeds 1×10^6 cycles, the degradation in the LRS is observed under RESET pulse A. The tail in HRS distribution indicates the decrease of cell resistance in part of the PCM cells which is induced by the over-programming effect, as shown in Fig. 3g. It suggests that the over-programming effect induced by the RESET pulse A leads to noticeable deterioration of the uniformity in the local atomic structure and composition of the phase change material as the endurance cycles increases. The uniformity of cell resistance is significantly improved both in the HRS and LRS of PCM cells under RESET pulse G, see Fig. 3h, which shows a resistance ratio of more than 100 after up to 1×10^9 endurance cycles. It is worthy of noting that the RESET pulse G exerts a comparatively limited influence on the threshold switching during the current sweeping of the PCM cells up to 1×10^{11} cycles. The resistance drift of both the HRS and LRS after different cyclic programmings of up to 1×10^9 cycles keeps relatively stable, as demonstrated in Figs. S7 and S8 in Supplementary Information.

Microstructural analysis on the atomic structure of PCM cells after cyclic switching

The cross-sectional TEM images of the PCM cells programmed under the RESET pulse A and pulse G for different endurance cycles are presented in Fig. 4a, b, respectively. The associated dark-field scanning transmission electron microscopy (DF-STEM) analysis is shown in Fig. 4c, d, respectively. The active switching region with a mushroom-like shape is observed in the phase change layer in all PCM cells. The active volumes are outlined by the dome-like materials with lighter contrast in the TEM images, irrespective of programming pulses and endurance cycles, which indicates a massive atomic segregation in the CGST phase change material during the cyclic switching. The size of the active switching region under RESET pulse A and pulse G is evaluated by normalizing the diameter of the active volume to the PCM cell that experienced 1×10^3 endurance cycles, as shown in Fig. 4a, b. When RESET pulse A is used in the cyclic programming, the size of the active volume decreases considerably by half as the switching endurance reaches 1×10^8 cycles, as shown in Fig. 4a(VI). While under RESET pulse G in the cyclic programming, the size of the active switching region remains stable until 10^9 switching cycles, which, after 1×10^{10} switching cycles, decreases slightly to 80% of the PCM cell that experienced 1×10^3 endurance cycles as given in Fig. 4b(VIII).

The segregated volume with lighter TEM contrast, which is defined as the core volume, is observed within the active region of the PCM cells under both RESET pulse A and pulse G in addition to the ones located at the dome-like boundaries, as presented in Fig. 4a, b. The appearance of the segregated core volumes is attributed to the presence of lighter or thinner phase change material under the driving forces in the cyclic switching, which implies the kernel of the heated active volume[10]. The core volumes within the active regions are marked by the orange circle in the DF-STEM images, as shown in Fig. 4c, d. The randomly distributed core volumes with various sizes after different switching cycles is observed inside the active region of PCM cells programmed by RESET pulse A, see Fig. 4c. The core volume eventually disappears as the switching endurance reaches 1×10^7 cycles due to the massive carbon segregation, as shown in Fig. 4c(V) and (VI). As the switching endurance cycle increases, the core volume identified in Fig. 4c migrates from the position next to the TiN heater to the top of the switching region with increased size which is attributed to the over-programming effect in the cyclic switching. While, as shown in Fig. 4d, the core volumes with uniform size are found to be located

close to the bottom TiN heater as the switching endurance increased to 1×10^9 cycles with RESET pulse G, indicating the effective suppression of the over-programming effect in the RESET programming.

The electron energy loss spectroscopy (EELS) analysis of carbon element in the PCL is shown in Fig. 4e, in which the carbon atoms present an explicit segregation at the boundary of the active volume. The carbon cluster that is located well above the interface to the dielectric layer outlines the dome-like shape of the switching region. It indicates that the active switching region predominantly resides within the phase change materials with the main path of current flow occurring from the embedded TiN heater toward the top electrode, as shown in the finite element simulation results of RESET process of the PCM cell, see Fig. S9 in Supplementary Information. Consequently, the Joule heat is largely confined in the vicinity between the TiN heater and the top electrode. A thicker segregated carbon cluster is recognized surrounding the active region of the PCM cell as the cyclic programming with RESET pulse A increases, see Fig. 4e(III). It leads to a significant reduction in the active volume after 1×10^8 endurance cycles. As the RESET pulse G is employed in the cyclic switching, a reduced degree of carbon accumulation at the boundary is observed after 1×10^7 and 1×10^8 endurance cycles, as depicted in Fig. 4e(IV) and (V). The carbon aggregation remains relatively weak before reaching 1×10^9 cycles after which significant carbon precipitation occurs inside the mushroom-like active region as confirmed by the chemical analysis results in Fig. S10 in Supplementary Information. The EELS mappings in Fig. 4e further confirm that the size of the active volume is less dependent on the programming history under RESET pulse G, even up to 1×10^{10} cycles, as shown in Fig. 4e(IV) to (VII).

Moreover, the energy dispersive x-ray spectroscopy (EDS) results in Fig. 4f, g demonstrates again the accumulation of carbon atoms and the associated depletion of Ge, Sb, and Te atoms at the boundary of the active region of PCM cells after 1×10^9 and 1×10^{10} switching cycles, respectively, under RESET pulse G. The presence of the constituent elements of CGST material is confirmed in the core volume of the PCM cells. The atom migration is observed as a local enrichment for Sb and depletion for Ge at the position close to the TiN heater as marked in Fig. 4f, g which is agreed with the reported publication[25,49,50]. It is worth mentioning that no Ti atoms were observed in the active volume of the phase change layer, suggesting a stable TiN heater in the cyclic switching. Indeed, the TiN heater remains in crystalline phase in both the survived and failed PCM cells as displayed in the high-resolution transmission electron microscopy (HRTEM) images in Fig. S11 in Supplementary Information. It indicates that the stuck-RESET failure should not be ascribed to the degradation of the bottom heater since a writing endurance of 1×10^{12} cycles is observed in the TiN bottom heater[51].

The carbon segregation is observed in the PCM cells immediately after the initialization test of hundreds of switching cycles is performed, as shown in Figs. 5a and S12 in Supplementary Information. In Fig. 5b, the large core switching volume in the top of the active region indicates a massive carbon aggregation after 1×10^6 switching cycles under RESET pulse A. As the switching endurance increases to 1×10^8 cycles, a remarkable shrink in the size of the active volume is observed with thicker carbon cluster piling up at the boundary, as shown in Fig. 5c. At the 3E8 switching cycles where the stuck-RESET failure occurs due to the over-programming effect, the continuous segregation of carbon atoms to the bottom heater and the resultant collapse of the active volume is observed in Figs. 5d and S10 in Supplementary Information. The over-programming effect is further confirmed by the horizontal expansion of the active region, in which the phase change material locates beyond the active region is in an amorphous state after 1×10^8 switching cycles under RESET pulse A. Whereas, under RESET pulse G, the phase change material in similar location remains intact showing a polycrystalline state, as shown in Fig. S13 in Supplementary Information.
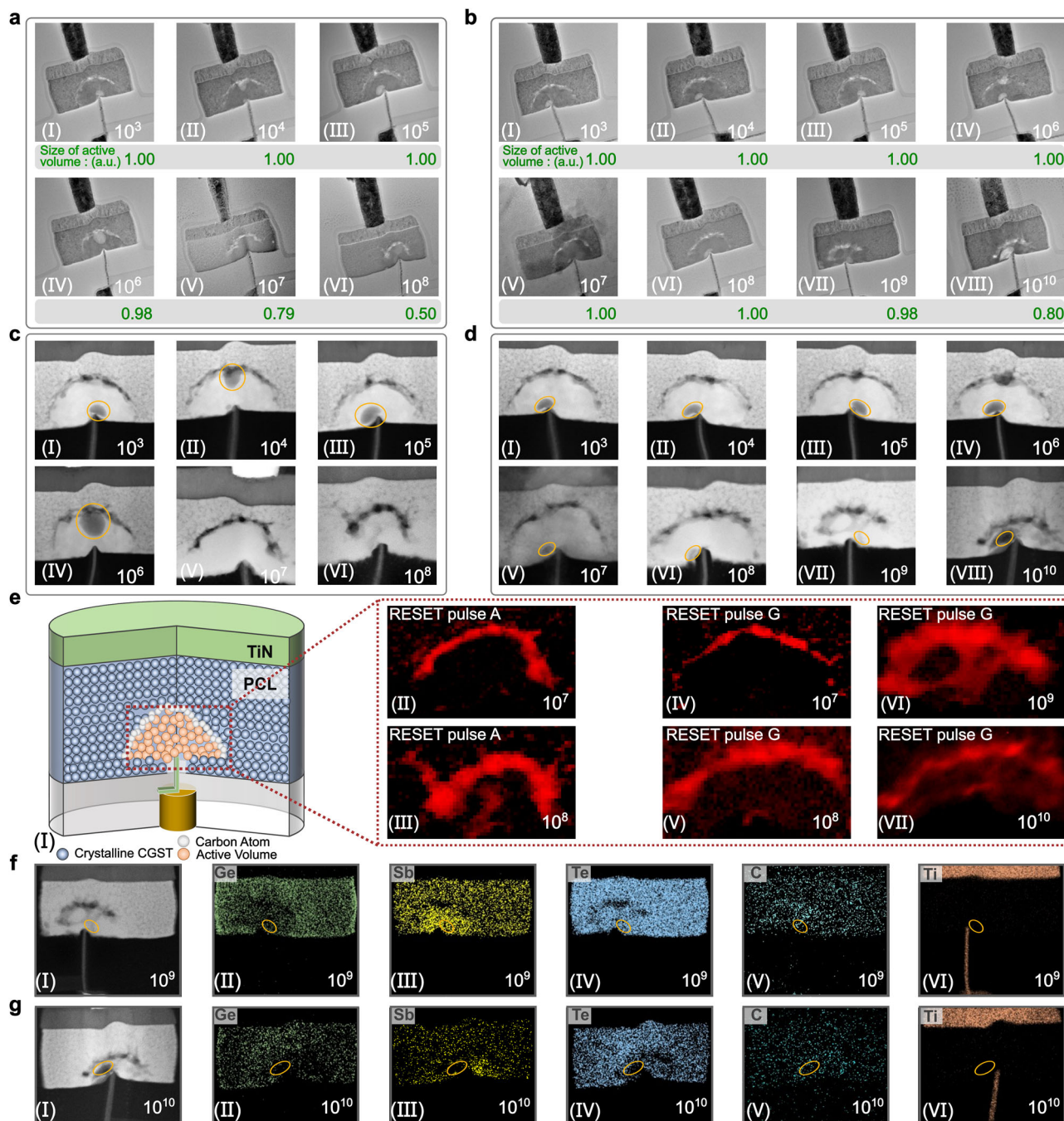
Fig. 4 | Microstructural analysis and elemental mappings of phase change memory (PCM) cells under various RESET pulses and cycling conditions. a The cross-sectional transmission electron microscopy (TEM) images of PCM cells programmed with RESET pulse A for (I) 10^3, (II) 10^4, (III) 10^5, (IV) 10^6, (V) 10^7, and (VI) 10^8 cycles. **b** The cross-sectional TEM images of PCM cells programmed with RESET pulse G for (I) 10^3, (II) 10^4, (III) 10^5, (IV) 10^6, (V) 10^7, (VI) 10^8, (VII) 10^9, and (VIII) 10^{10} cycles. The corresponding cross-sectional dark-field scanning transmission electron microscopy images of PCM cells programmed with **c** RESET pulse A and **d** RESET pulse G where the core volume is marked by orange circles. **e** The carbon atom distribution in the phase change layer, though electron energy loss spectroscopy (EELS) analysis with focus on (I) the active volume. The carbon segregation revealed by EELS mapping for the PCM cells programmed by RESET pulse A for (II) 10^7 and (III) 10^8 cycles and by RESET pulse G for (IV) 10^7, (V) 10^8, (VI) 10^9, and (VII) 10^{10} cycles. The energy dispersive x-ray spectroscopy mapping of the PCM cells programmed by RESET pulse G for (**f**) 10^9 and (**g**) 10^{10} cycles where the core volume is outlined by orange circles.

The RESET pulse A in the cyclic programming exacerbates the carbon segregation process due to the over-programming effect, which involves the driving forces from the incongruent melting and electrostatic force in the cyclic switching[10,20–25]. The EDS results shown in Figs. S14 and S15 in Supplementary Information demonstrate the enrichment of carbon atoms at the boundary of the active volume where the Ge, Sb, and Te elements are scarcely detected. Consequently, the additional cyclic switching leads to the formation of a

thicker carbon cluster at the boundary of the active volume, which progressively migrates toward the bottom heater and accelerates the failure of the PCM cell by crushing the active volume. Moreover, the recrystallization of phase change material was observed at the outer periphery of the active region. It is due to the over-programming effect, which gives rise to the formation of crystalline phase change material at the boundary of active volume and subsequently squeezes the size of the switching region, see Fig. S16 in Supplementary
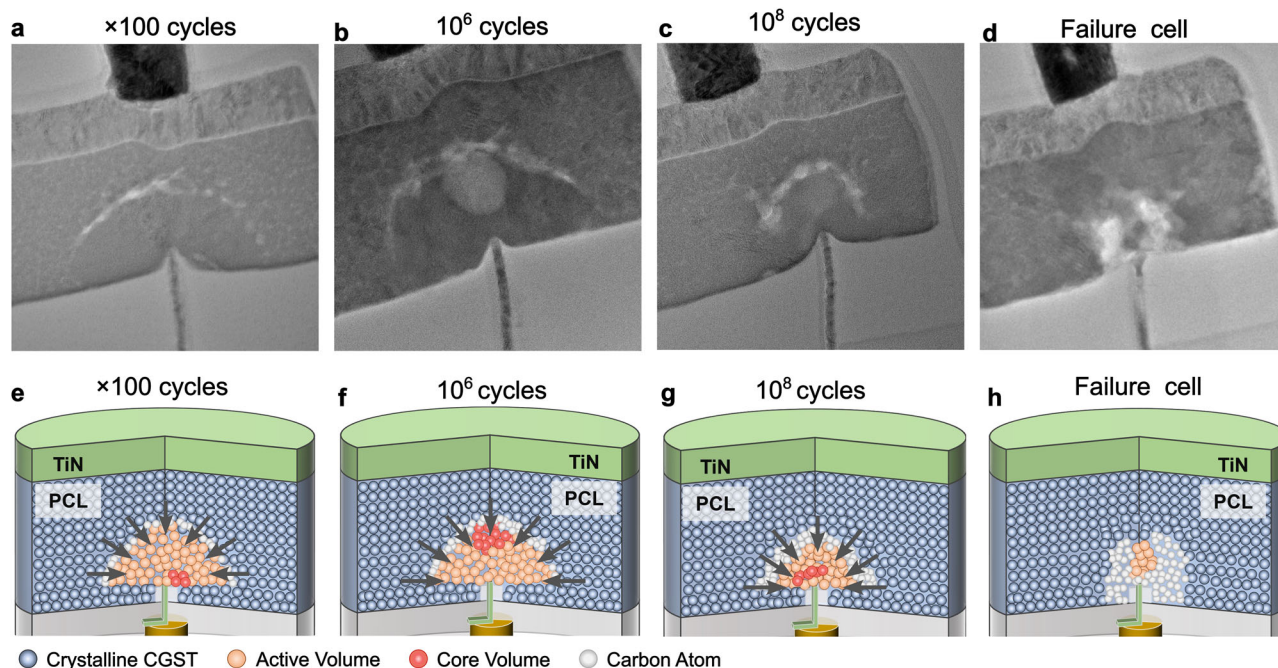
Fig. 5 | Evolution of active volume and carbon segregation in phase change layer (PCL) of phase change memory (PCM) cells under RESET pulse A with increasing endurance cycles. The high-resolution transmission electron microscopy images of the active volume of the PCM cells programmed by RESET pulse A for **a** ×100, **b** 10^6, **c** 10^8, and **d** 10^9 cycles. **e–h** The cartoon of the evolution of the active volume (marked by the orange balls) of the PCM cells programmed by RESET pulse A with increased endurance cycles, where the shrinkage of the active region results from the substantially increased carbon segregation with cycles at the boundary. The core volume (marked by the red balls) is randomly distributed in the active volume as the endurance cycle increased. The segregated carbon atoms (marked by the white balls) lead to the collapse of active volume, eventually giving rise to the open state of the PCM cells with a stuck-RESET failure.

Information. The failed PCM cell is characterized by a collapsed active switching volume, which is filled with the segregated carbon atoms that envelop the TiN heater as presented in Fig. S10 in Supplementary Information. It thus leads to an open state of the PCM cell with stuck-RESET failure, as illustrated in Fig. 5e–h.

Discussion

In this work, we propose a mushroom-type nano-confined cell structure, which enables RESET switching operation with significantly reduced program energy. Our approach provides a highly scalable, cost-effective, and thermally optimized solution compared to the confined PCM cells by ALD process. The endurance performance of the PCM cells is significantly extended beyond 1.1×10^{11} switching cycles by taking advantage of reduced programming energy that mitigates the over-programming effect caused by the excessive RESET current. The RESET pulse with significantly reduced energy is capable of curing the active volume of the PCM cells in the cyclic switching, which enables long post-endurance reversible switching.

The microstructural analysis on the post-endurance PCM cells reveals the immediate carbon segregation at the boundary of the active switching volume after hundreds of cycles. The massive carbon precipitation is accelerated with the increase of switching cycles, which presents a path toward the bottom heater due to the recrystallization of the phase change material. It leads to significant shrinkage of the active volume and finally the collapse of the active region of the PCM cells. The nano-confined structure effectively addresses the over-programming issues by relocating the melt-quench region away from the interface to the dielectric layer, in which the thermal efficiency can be further enhanced by tuning the structure of the bottom heater in the PCL. This work reveals that a stable active volume of phase change material is crucial for extending the endurance limits of PCM cell. The optimization of programming parameters to suppress the over-programming effect and the continuous scaling in cell size to

reduce the active volume are considered as essential ways to further stabilize the segregated dome-like carbon cluster, thus enabling the active volume with extended endurance cycles. The memory cell with embedded nano-heater could be taken by other emerging memristive devices directly to trigger the resistive switching at the atomic scale with low switching power and long switching endurance.

Methods

Device fabrication and simulation

The conventional and nano-confined PCM cells were fabricated on a 12-inch silicon substrate using a 40 nm technology with one transistor one resistance memory architecture. All the devices used in this work consist of a TiN bottom heater, CGST phase change layer, and TiN top electrode. The PCM device adopts a mushroom-type cell structure. The details of the conventional cell structure can be found in previous publications[7,52]. For the nano-confined cell structure an embedded bottom TiN heater was formed by ALD process, which is followed by a recess process via selective chemical mechanical planarization (CMP) to form a protruded bottom heater. The ALD-deposited TiN film is capped by SiN layer to avoid oxidation of TiN bottom heater. It also ensures that the PCL is only in contact with the top surface of the TiN bottom heater. For the fabrication of nano-confined structures, the degree of protrusion of TiN bottom heater is optimized by tuning the CMP process. The slurry used in the CMP process shows a good selectivity between the TiN and SiO_2 material. By controlling the polishing time, the protrusion degree and height of the TiN bottom heater can be tuned. The CGST phase change layer was deposited by magnetron sputtering, which allows for greater flexibility in material composition and avoids contamination from residual by-products that exist in the chemical deposition method. The CGST composition was optimized to increase thermal stability and reduce operation energy, which are critical for long-term endurance[7,18]. The top TiN electrode was subsequently deposited using the PVD method right after the

deposition of the phase change material to avoid oxidation. The CGST phase change layer is patterned by plasma etching, which is followed by the deposition of SiN interlayer dielectric via a low-temperature chemical vapor deposition technique. The finite element model was established using COMSOL Multiphysics software, incorporating an electrical model coupled with a thermal model through Joule heating. Heat transfer via conduction is simulated using the transient heat equation, in which a constant RESET pulse is applied to the PCM cells with a flat or embedded TiN heater.

Microstructural analysis

The cross-sectional TEM samples of the PCM cells are prepared using a Helios G4 UX dual-beam focus ion beam (FIB) system with a Ga ion beam operated at 30 kV acceleration voltage and polished at 5 kV. The final thinning and cleaning process is performed at 2 kV to minimize the damage to the sample. The beam current in the TEM analysis is reduced to around 1 nA to avoid the electron irradiation-induced amorphous to crystalline phase transition of the lamellae. The DF-STEM image and the associated EDS experiments were performed on a JEOL ARM300F microscope at 300 kV with a low beam intensity. No visible structural changes are observed in the DF-STEM and EDS experiments. The high spatial resolution chemical analysis of carbon atoms in the active volume of the PCM cell is carried out by EELS mapping at an energy resolution of 1 eV/channel.

Electrical measurements

All electrical measurements were performed at the chip level using automatic test equipment (ATE). The customized circuit boards and sockets are used to ensure direct electrical contact with the PCM chips.

The RESET and SET operations of the PCM devices were conducted through the on-chip write circuit. The on-chip write circuit was configured via the ATE tester, which defines the duration and amplitude of the RESET and SET pulses. The duration of the RESET pulse depends on the configuration of on-chip write circuit. In this work, eight different RESET pulses (RESET Pulse A to H) corresponding to pulse widths of 20 ns, 15 ns, 10 ns, 9 ns, 8 ns, 7 ns, 6 ns, and 5 ns, respectively, are used. The amplitude of each RESET pulse was 1000 μA in the endurance switching measurement. Although a RESET current of 7 ns, 500 μA is able to program the HRS of PCM cell as shown in the main text, the RESET current of 1000 μA is selected in order to ensure good overall performance on data retention, device consistency, and higher on/off ratio of the PCM devices. The SET pulse duration and current were fixed at 440 ns and 400 μA, respectively.

The endurance testing was conducted using the ATE system via a dedicated endurance test program, which is achieved by repeatedly writing data '0' (RESET) and data '1' (SET) to the selected memory address. The measurement of the cell resistance is performed after every 1×10^5 cycles of RESET and SET operations. The drift coefficient of cell resistance was extracted by fitting the resistance-time curve to the power law $R(t) = R_0(t/t_0)^\nu$ where ν is drift coefficient and R_0 is the resistance measured at time t_0. Additionally, the distribution of cell resistance across multiple cycles and devices was analyzed based on 8192 (8k array) PCM devices to demonstrate the reliable switching performance of the nano-confined structure.

Data availability

All data that support the findings of this study are included in the main text and Supplementary Information. Other data are available from the corresponding author upon request.

References

1. Lanza, M. et al. Memristive technologies for data storage, computation, encryption, and radio-frequency communication. *Science* **376**, eabj9979 (2022).
2. Qiu, J., Wu, Q., Ding, G., Xu, Y. & Feng, S. A survey of machine learning for big data processing. *EURASIP J. Adv. Signal Process.* **2016**, 1–16 (2016).
3. Pacchioni, G. Data storage: a diamond bit is forever. *Nat. Rev. Mater.* **1**, 1 (2016).
4. Sebastian, A., Le Gallo, M., Khaddam-Aljameh, R. & Eleftheriou, E. Memory devices and applications for in-memory computing. *Nat. Nanotechnol.* **15**, 529–544 (2020).
5. Grossier, N. et al. ASIL-D automotive-grade microcontroller in 28nm FD-SOI with full-OTS capable 21MB embedded PCM memory and highly scalable power management. In *2023 IEEE Symposium on VLSI Technology and Circuits (VLSI Technology and Circuits)*, 1–2 (IEEE, 2023).
6. Rao, F. et al. Reducing the stochasticity of crystal nucleation to enable subnanosecond memory writing. *Science* **358**, 1423–1427 (2017).
7. Song, Z. et al. High endurance phase change memory chip implemented based on carbon-doped $Ge_2Sb_2Te_5$ in 40 nm node for embedded application. In *2018 IEEE International Electron Devices Meeting (IEDM)*, 27–5 (IEEE, 2018).
8. Cheng, H. et al. New phase-change materials by atomic-level engineering the dopants for extremely low V_{th} drift at 85 °C and high endurance 3D crosspoint memory. In *2022 International Electron Devices Meeting (IEDM)*, 18–5 (IEEE, 2022).
9. Fazio, A. Advanced technology and systems of cross point memory. In *2020 IEEE International Electron Devices Meeting (IEDM)*, 24–1 (IEEE, 2020).
10. Kim, S., Burr, G. W., Kim, W. & Nam, S.-W. Phase-change memory cycling endurance. *MRS Bull.* **44**, 710–714 (2019).
11. Khan, A. I. et al. Energy efficient neuro-inspired phase change memory based on $Ge_4Sb_6Te_7$ as a novel epitaxial nanocomposite. *Adv. Mater.* **35**, 2300107 (2023).
12. Arnaud, F. et al. High density embedded PCM cell in 28nm FDSOI technology for automotive micro-controller applications. In *2020 IEEE International Electron Devices Meeting (IEDM)*, 24–2 (IEEE, 2020).
13. Xie, Y. et al. Self-healing of a confined phase change memory device with a metallic surfactant layer. *Adv. Mater.* **30**, 1705587 (2018).
14. Sky, M. B. et al. Crystalline-as-deposited ALD phase change material confined PCM cell for high density storage class memory. In *2015 IEEE International Electron Devices Meeting (IEDM)*, 3.6.1–3.6.4 (2015).
15. Kim, W. et al. ALD-based confined PCM with a metallic liner toward unlimited endurance. In *2016 IEEE International Electron Devices Meeting (IEDM)*, 4.2.1–4.2.4 (2016).
16. Ranica, R. et al. Heater system optimization for robust ePCM reliability and scalability in 28nm FDSOI technology. In *2021 IEEE International Electron Devices Meeting (IEDM)*, 28–1 (IEEE, 2021).
17. Redaelli, A. et al. Beol process effects on ePCM reliability. *IEEE J. Electron Devices Soc.* **10**, 563–568 (2022).
18. Zhou, X. et al. Carbon-doped $Ge_2Sb_2Te_5$ phase change material: a candidate for high-density phase change memory application. *Appl. Phys. Lett.* **101**, 142104 (2012).
19. Zhou, X. et al. Understanding phase-change behaviors of carbon-doped $Ge_2Sb_2Te_5$ for phase-change memory application. *ACS Appl. Mater. Interfaces* **6**, 14207–14214 (2014).
20. Ahn, S. J. et al. Reliability perspectives for high density PRAM manufacturing. In *2011 International Electron Devices Meeting*, 12.6.1–12.6.4 (2011).
21. Chen, C.-F. et al. Endurance improvement of $Ge_2Sb_2Te_5$-based phase change memory. In *2009 IEEE International Memory Workshop*, 1–2 (IEEE, 2009).
22. Nam, S.-W. et al. Electrical wind force–driven and dislocation-templated amorphization in phase-change nanowires. *Science* **336**, 1561–1566 (2012).

23. Lee, M. et al. The impact of hole-induced electromigration on the cycling endurance of phase change memory. In *2010 International Electron Devices Meeting*, 28.6.1–28.6.4 (2010).

24. Rizzi, M. et al. Intrinsic retention statistics in phase change memory (PCM) arrays. In *2013 IEEE International Electron Devices Meeting*, 21.7.1–21.7.3 (2013).

25. Nam, S.-W. et al. Phase separation behavior of $Ge_2Sb_2Te_5$ line structure during electrical stress biasing. *Appl. Phys. Lett.* **92**, 111913 (2008).

26. Kim, W. et al. Reliability benefits of a metallic liner in confined PCM. In *2018 IEEE International Reliability Physics Symposium (IRPS)*, 6D–5 (IEEE, 2018).

27. Adinolfi, V. et al. Composition-controlled atomic layer deposition of phase-change memories and ovonic threshold switches with high performance. *ACS Nano* **13**, 10440–10447 (2019).

28. Chen, Z. et al. High-performance HfO_x/AlO_y-based resistive switching memory cross-point array fabricated by atomic layer deposition. *Nanoscale Res. Lett.* **10**, 1–7 (2015).

29. Wang, H. et al. Fast and scalable phase change materials Ti–Sb–Te deposited by plasma-enhanced atomic layer deposition. *J. Mater. Sci.: Mater. Electron.* **31**, 5833–5837 (2020).

30. Park, E.-S. et al. Atomic layer deposition of nanocrystalline-as-deposited $(GeTe)_x (Sb_2Te_3)_{1-x}$ films for endurable phase change memory. *Chem. Mater.* **31**, 8752–8763 (2019).

31. Lee, Y. K., Yoo, C., Kim, W., Jeon, J. W. & Hwang, C. S. Atomic layer deposition of chalcogenides for next-generation phase change memory. *J. Mater. Chem. C.* **9**, 3708–3725 (2021).

32. Laudato, M. et al. Ald geassete ovonic threshold switch for 3D stackable crosspoint memory. In *2020 IEEE International Memory Workshop (IMW)*, 1–4 (IEEE, 2020).

33. Eom, T. et al. Conformal formation of $(GeTe_2)_{(1-x)}(Sb_2Te_3)_x$ layers by atomic layer deposition for nanoscale phase change memories. *Chem. Mater.* **24**, 2099–2110 (2012).

34. Pore, V., Hatanpaa, T., Ritala, M. & Leskela, M. Atomic layer deposition of metal tellurides and selenides using alkylsilyl compounds of tellurium and selenium. *J. Am. Chem. Soc.* **131**, 3478–3480 (2009).

35. Gwon, T. et al. Atomic layer deposition of GeTe and Ge–Sb–Te films using $HGeCl_3$, $Sb (OC_2H_5)_3$, and $\{(CH_3)_3Si\}_2Te$ and their reaction mechanisms. *Chem. Mater.* **29**, 8065–8072 (2017).

36. Kim, T. et al. High-performance, cost-effective 2z nm two-deck cross-point memory integrated by self-align scheme for 128 Gb scm. In *2018 IEEE International Electron Devices Meeting (IEDM)*, 37–1 (IEEE, 2018).

37. Canvel, Y. et al. Modification of Ge-rich GeSbTe surface during the patterning process of phase-change memories. *Microelectron. Eng.* **221**, 111183 (2020).

38. Hong, S. et al. Extremely high performance, high density 20nm self-selecting cross-point memory for compute express link. In *2022 International Electron Devices Meeting (IEDM)*, 18–6 (IEEE, 2022).

39. Zhou, W. et al. Increasing lifetime and security of phase-change memory with endurance variation. In *2016 IEEE 22nd International Conference on Parallel and Distributed Systems (ICPADS)*, 861–868 (2016).

40. Niu, D., Chen, Y., Dong, X. & Xie, Y. Energy and performance driven circuit design for emerging phase-change memory. In *2010 15th Asia and South Pacific Design Automation Conference (ASP-DAC)*, 193–198 (2010).

41. Kim, K. & Ahn, S. J. Reliability investigations for manufacturable high density PRAM In *2005 IEEE International Reliability Physics Symposium, 2005. Proceedings. 43rd Annual.*, 157–162 (2005).

42. Ha, D. & Kim, K. Recent advances in high density phase change memory (PRAM). In *2007 International Symposium on VLSI Technology, Systems and Applications (VLSI-TSA)*, 1–4 (2007).

43. Jiang, L., Zhang, Y. & Yang, J. Enhancing phase change memory lifetime through fine-grained current regulation and voltage upscaling. In *IEEE/ACM International Symposium on Low Power Electronics and Design*, 127–132 (2011).

44. Chao, D.-S. Investigation of coupling characteristics of series-connected phase-change memory cells varied in programmable volume. *Appl. Phys. Express* **12**, 085002 (2019).

45. Cho, S. et al. Highly scalable on-axis confined cell structure for high density pram beyond 256Mb. In *Digest of Technical Papers. 2005 Symposium on VLSI Technology*, 96–97 (2005).

46. Matsui, Y. et al. Ta_2O_5 interfacial layer between GST and W plug enabling low power operation of phase change memories. In *2006 International Electron Devices Meeting*, 1–4 (2006).

47. Baek, K. et al. Microstructure-dependent dc set switching behaviors of Ge–Sb–Te-based phase-change random access memory devices accessed by in situ TEM. *NPG Asia Mater.* **7**, e194 (2015).

48. Cheng, Y. et al. Microscopic mechanism of carbon-dopant manipulating device performance in CGeSbTe-based phase change random access memory. *ACS Appl. Mater. Interfaces* **12**, 23051–23059 (2020).

49. Novielli, G., Ghetti, A., Varesi, E., Mauri, A. & Sacco, R. Atomic migration in phase change materials. In *2013 IEEE International Electron Devices Meeting*, 22.3.1–22.3.4 (2013).

50. Rajendran, B. et al. On the dynamic resistance and reliability of phase change memory. In *2008 Symposium on VLSI Technology*, 96–97 (2008).

51. Wan, Z. et al. High endurance nanoscale TiN bottom heater for phase change memory. In *2025 9th IEEE Electron Devices Technology & Manufacturing Conference (EDTM)* (2025).

52. Lu, Y. et al. Accelerated local training of CNNs by optimized direct feedback alignment based on stochasticity of 4 Mb C-doped $Ge_2Sb_2Te_5$ PCM chip in 40 nm node. In *2020 IEEE International Electron Devices Meeting (IEDM)*, 36.3.1–36.3.4 (IEEE, San Francisco, CA, USA, 2020).

Acknowledgements

Author contributions

The project was initiated and conceptualized by X. Zh. and Z.S. X. Zh., J. Zheng and R.W. designed the experiments and drafted the manuscript. L.X., Q.W. and X.L. designed the circuits. W.F., C.L., J. Zheng, J.Z., Z.W., Y.C., J.L. and X.Z. Fabricated the memory device array and carried out the integration with CMOS. X.Zh. performed the finite element simulation. R.W., S.S. and X.Zh. analyzed the TEM results. L.X., J.Zheng and X.L. performed the electrical measurements. All authors discussed the results and contributed to the manuscript at all stages.

Competing interests

The authors declare no competing interests.

Additional information

Supplementary information The online version contains supplementary material available at https://doi.org/10.1038/s41467-025-60644-1.

Correspondence and requests for materials should be addressed to Xilin Zhou or Zhitang Song.

Peer review information *Nature Communications* thanks Kristy Campbell, and the other, anonymous, reviewer(s) for their contribution to the peer review of this work. A peer review file is available.

Reprints and permissions information is available at http://www.nature.com/reprints

Publisher's note Springer Nature remains neutral with regard to jurisdictional claims in published maps and institutional affiliations.